Available online at www.sciencedirect.com
ScienceDirect
Trans. Nonferrous Met. Soc. China 34(2024) 2275−2288
Transactions of Nonferrous Metals Society of China
www.tnmsc.cn

Plasma-sprayed Al-based coating with WC-addition for excellent corrosion resistance and enhanced wear protection of Mg alloys

Haroon RASHID, Xiao-tao LUO, Xin-yuan DONG, Li ZHANG, Chang-jiu LI

State Key Laboratory for Mechanical Behavior of Materials, School of Materials Science and Engineering, Xi'an Jiaotong University, Xi'an 710049, China

Received 6 January 2023; accepted 10 September 2023

Abstract: Thermal spray processes struggle to create a fully dense coating for corrosion protection in the as-sprayed state due to the poor inter-splat bonding. To tackle this problem, Al−15vol.%WC was utilized as the coating material and applied by atmospheric plasma spraying (APS) to produce a dense coating with self-metallurgical inter-splat bonding. The results show that due to the in-flight particle deoxidizing effect by C element and self-metallurgical bonding of the overheated droplet (>1800 °C), dense coating without oxides inclusions is produced under optimized plasma spraying conditions. The fully dense Al−WC coating exhibits excellent corrosion resistance, with corrosion current density lower by four and two orders than that of Mg alloy substrate and bulk Al, respectively. Due to the inclusion of hard WC particles, the Al−WC coating presents one order improvement in wear resistance compared with the bulk Al.
Key words: atmospheric plasma spray (APS); Al−WC coating; self-metallurgical bonding; deoxidization effect; corrosion resistance; wear resistance

1 Introduction

Magnesium alloys are considered a good choice for applications in various fields due to the high specific strength. However, their low corrosion resistance and wear resistance limit their applications [1,2]. To protect a material against surface deteriorating factors like corrosion and wear, commonly adopted strategies include an internal change, like modification of the composition of the material or modification of the surface composition and an external change like application of a coating. Instead of altering the composition of the entire material, applying a protective coating is a more cost-effective approach. Amongst various surface protection techniques used for Mg alloys [3], thermal plasma spray coating method has also proven its worth in terms of flexibility of the material selection, variable coating microstructure, variable thickness and high deposition rate [3]. DAROONPARVAR et al [4] have given a good review on surface modification of Mg alloys using thermal spray processes. The reinforced aluminum coating can help increase the wear and corrosion resistance of Mg, which is the focus of this research work.

Thermal spray coatings differ from their bulk counterparts and other types of coatings due to their unique lamellar structure, porosity, oxide inclusions, and unmelted particles [5,6]. The limited bonding between individual lamella interfaces not only permits the penetration of corrosive substance to the coating/substrate interface, but also reduces wear performance [7,8]. Therefore, as corrosion protective coatings, they should be sealed prior to

Corresponding author: Chang-jiu LI, Tel: +86-29-82660970, E-mail: licj@mail.xjtu.edu.cn;
Xiao-tao LUO, E-mail: luoxiaotao@mail.xjtu.edu.cn
DOI: 10.1016/S1003-6326(24)66540-4

service. However, pore sealing treatment by organic sealants is not cost-effective and durable. Moreover, the sealants could only penetrate to a limited top layer of the coating, which can be removed by abrasion. Pore sealing is only effective in the absence of substantial abrasion. As a result, thermal spray processes need improvement to prepare fully dense bulk-like coatings [9]. The ability of the plasma spray method to create bulk-like coatings has recently been demonstrated through the plasma spray of low melting point self-fluxing alloys [10] and by the in-flight deoxidizing effect of specific sacrificial elements included in spray powder [11], as reported by ZENG et al [12]. It has been mentioned [11] that plasma spray has an advantage over the flame spray method because through efficient use of high temperature, plasma spray particles can be heated to highly overheated temperatures that are essential for starting both the in-flight deoxidizing effect and spread-fusing self-bonding mechanism [9]. In our previous study [13], for carbon-containing alloys such as NiAl, it was found that the carbon element can be used as an in-flight in-situ deoxidizer to suppress the oxidation of aluminum.

In this work, it is attempted to deposit corrosion- and wear-resistant coating through alteration of feedstock powder without any post-spray coating treatments by plasma spray. WC particles were added to Al matrix to introduce deoxidizer carbon and reinforcing phase. Al composite powder particles were utilized for atmospheric plasma spraying to prepare the WC-reinforced Al coatings to aim at achieving the composite coating with high cohesion and high hardness besides its excellent corrosion resistance.

2 Experimental

2.1 Materials preparation

The Al−15vol.%WC (Al−WC) and pure Al powders were used for the deposition of atmospheric plasma spray (APS) coatings. Both powders were in a size range of 50−100 μm. Al−WC powder was prepared by mechanical alloying through planetary ball milling by adding 15 vol.% of 2 μm WC particles in Al particles. The Al and WC powders were first mixed for 1 h in an automatic mixer to obtain a uniform mixture. Then, the powder mixture was milled in a planetary ball mill by using hardened stainless steel vials and balls in an inert argon atmosphere to minimize the oxidation of powders. The ball-to-powder mass ratio was 10:1, and the ball milling was performed at a rotation speed of 180 r/min and the total milling time was 120 min. Figure 1 shows the morphology and cross-sectional microstructure of the WC−Al composite powder. In the SEM images taken in a back-scattered electron mode (Fig. 1(b)), it can be seen that small-sized bright WC particles are homogeneously distributed in a greyish Al matrix and the milled powder presents an irregular shape. The density of composite Al−WC particles is 4.64 g/cm^3, being higher than the density of pure Al particles, i.e. 2.7 g/cm^3.

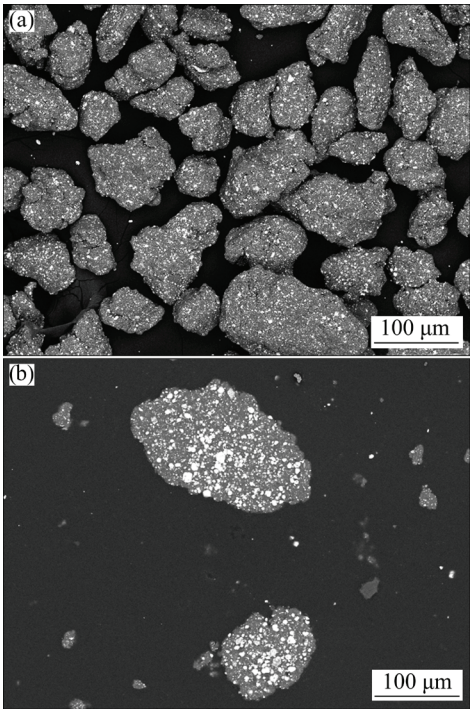

Fig. 1 Surface morphology (a) and cross-sectional structure (b) of Al−WC powder

2.2 Particle velocity and temperature measurement

The in-flight particle temperature and velocity of the APS prepared Al and Al−WC powder particles were measured at the center line of the flow, using a commercial thermal spray particle diagnostic system (DPV−2000, Tecnar Automation Ltd., St-Bruno, Québec, Canada). During the test, the detector was focused perpendicularly on the sprayed stream of particles at the spray distance specified for coating deposition to measure the temperature and velocity of particles at this distance.

2.3 Preparation of coatings and single splats

APS prepared Al and Al−WC coatings were deposited on AZ31B Mg alloy substrate using a commercial plasma spraying system (80 kW, Jiujiang, China). The substrates were grit-blasted prior to spray to create a rough surface and thus improve the adhesion between the substrate and the coating. To clarify the bonding formation mechanism between adjacent deposited particles, isolated Al−WC splats were deposited on the polished Al7075 alloy substrates using the same APS system to analyze whether the impact of Al−WC particle melts the Al substrate or not for metallurgical bonding formation between splats. The parameters used for coatings and splat deposition are given in Table 1. The plasma torch was manipulated perpendicularly over the substrate by a robot to spray particle streams.

Table 1 Plasma spray parameters for coating and splat deposition

Parameter	Value
Plasma arc power/kW	30
Arc current/A	500
Arc power/V	60
Flow rate of plasma gas (Ar)/(L·min^{-1})	50
Flow rate of auxiliary gas (H_2)/(L·min^{-1})	2.5
Spray distance/mm	100
Step size/mm	3
Torch traverse speed/(mm·s^{-1})	450 for coating and 1000 for splat

2.4 Characterization of coatings and splats

The microstructures of both isolated splats and coatings were examined using scanning electron microscopy (SEM, MIRA 3 LMH, TESCAN, Czech). Energy dispersive spectroscopy (EDS) was used to analyze the element distribution within the coating. X-ray diffraction (XRD) and transmission electron microscopy (TEM) were performed to explore the microstructure of coatings. The image-analyzing method was used to estimate the apparent porosity of the coatings.

2.5 Tensile adhesive strength test

ASTM C633—13 standard was followed to measure the adhesion/cohesion of coatings and samples were prepared accordingly. Five identical cylinder couples were used for the test of each coating. One of the samples in each couple was grit blasted and covered with the coating and the other just grit blasted and was not coated. Both were glued to each other using a resin glue (Adbest, HUA YI Resins Co, Ltd.) which has a maximum tensile strength of ~70 MPa. The glued cylinders were mounted in a tensile test machine with a self-aligning fixture and pulled apart at a cross-head speed of 1 mm/min until the coating failed. The value of the load at fracture was noted for each sample.

2.6 Corrosion resistance tests

The electrochemical corrosion behavior of the coatings was tested using a CS310 electrochemical workstation (Corrtest Instruments Co., Ltd., Wuhan, China). Three-electrode electrochemical cell system was employed with a saturated calomel electrode (SCE) as the reference electrode and a platinum electrode as the counter electrode. The coated samples with coating thickness ranging from 300 to 350 μm acted as a working electrode (with square area exposed surface of 1.5 cm^2). The coating surface was polished before testing to smooth the surface irregularities. The electrolyte was 3.5 wt.% NaCl aqueous solution. For each sample, the open circuit potential (OCP) was measured firstly followed by the potentio-dynamic polarization (PDP) test by scanning from a cathodic potential toward an anodic potential, at a scanning rate of 0.5 mV/s. OCP and PDP curves of bulk Al alloy Al7075 and bulk Mg alloy AZ31B were also obtained to compare with Al and Al−WC coatings. Neutral salt-fog spray corrosion test was performed on Al-coated AZ31B alloy and Al−WC-coated AZ31B alloy. According to ASTM B117—16 standard, the samples were continuously exposed to 5 wt.% NaCl salt-fog spray at 35 °C for 1000 h in a salt fog chamber (YWX/Q−250, Yashilin Testing Equipment Co., Ltd., Beijing, China) with a relative humidity of 100%. Samples of both coatings were taken out for test after every 100 h.

2.7 Wear test

The abrasive wear behavior of the coatings was investigated using a pin-on-disk tribometer at room temperature under dry sliding conditions in comparison with that of AZ31B Mg alloy substrate. The test was conducted on CFT−1 material surface

comprehensive performance tester (Lanzhou Zhongke Kaihua Technology Development Co., Ltd., China). An alumina ball with a diameter of 6 mm was used as the friction counter body. The surface of the coating was polished prior to the wear test. All the tests were performed at a sliding speed of 105 mm/s and the applied load was 5 N. The coated samples were weighed before and after the test to estimate material loss during wear.

3 Results and discussion

3.1 Particle temperature and velocity

Since the overheated droplet is a necessary condition for the fully dense coating, the particle temperature and velocity were measured firstly. Figure 2 shows the in-flight particle temperature and velocity of the APS prepared Al and Al−WC powder particles having similar particle size distribution. The spray parameters of APS were the same for both powder particles. As shown in our previous work [9], when Al droplets are heated to a temperature higher than 1800 °C, their impact can cause spread-fusing of previously deposited Al splat surface, and subsequently lead to metallurgical bonding across the lamellar interface. It can be observed in Fig. 2, that most of the particles acquire a temperature higher than 1800 °C. Another critical observation from velocity comparison is that the velocities of Al−WC particles are slightly lower than those of Al particles because of the higher density. The lower velocity gives spray particles a longer dwelling time in plasma jet, which results in a slightly higher mean temperature of Al−WC particles than that of pure Al particles.

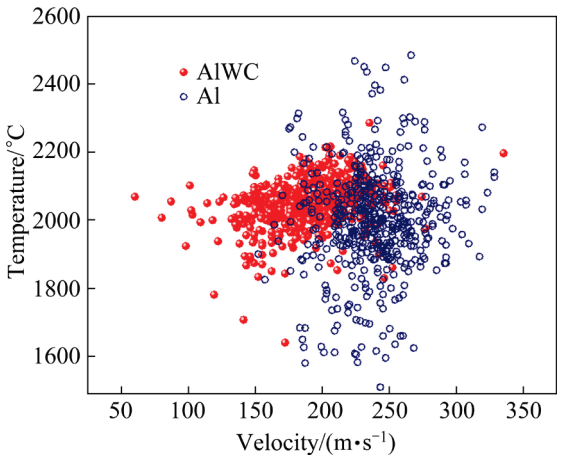

Fig. 2 Particle temperature and velocity of Al−WC particles vs Al particles

3.2 Interfacial microstructure of Al−WC single splats

It is difficult to observe particle impact-induced melting on the previously deposited surface of Al-based coating because of uneven rough surface morphology. Thus, a well-polished Al7075 alloy substrate with alloying elements that the powder does not have was chosen as a substrate to deposit isolated single splats so that, in the event that an Al particle melts the Al alloy substrate during spreading, the proof of melting could be obtained by EDS mapping of the cross-section of splat, including the splat−substrate interface. The flat substrate was well polished before spraying for splat deposition at a pre-heating temperature of 150 °C. To prevent surface adsorbates from causing splashing when the molten particles spread, the substrate temperature was elevated to 200 °C and subsequently lowered to 150 °C [14].

The cross-sectional microstructure of the deposited Al−WC single splat can be seen in Figs. 3(a, b). Substrate surficial melting-induced craters can be clearly observed at the splat−substrate

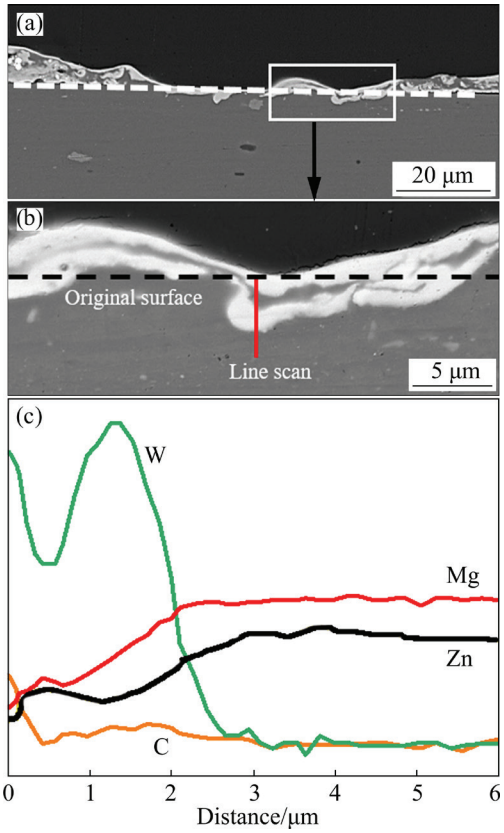

Fig. 3 Cross-sectional microstructure of Al−WC single splat at lower magnification (a) and higher magnification (b); EDS line scanning across Al−WC splat−substrate interface (c)

interface. As mentioned earlier, the surface of the substrate was polished before spray and therefore presented a flat profile. The white dotted reference line represents the pre-spray flat position of the substrate surface. After the splat was deposited, the splat−substrate interface presents a wavy profile, as shown in Fig. 3, due to melting at the point of splat impact. The distributions of alloying elements, Mg and Zn, by EDS line scanning, shown in Fig. 3(c), show a gradual rise in the concentration of these elements from the top surface to the substrate. This trend further confirms that a strong mixture of the splat with the substrate material occurred. Therefore, it is evident that the fusing of the substrate surface layer occurred by the impact of molten Al−WC droplet. As a result, splat containing certain amount of the substrate material was welded to the 7075Al substrate by metallurgical bonding.

These experimental results indicate that the inter-lamellar metallurgical bonding is possible in the aluminum-based coating when APS coating is deposited with the parameters under which the spray particles can be heated to a temperature higher than 1800 °C. A close observation of the peripheral regions of the single splat cross-sections in Fig. 3(a), clearly indicated that the splat was not well bonded in the peripheral region. This is because splat cools at a very rapid rate, and with the progress of spreading, melt temperature decreases rapidly. Accordingly, the melt at the spreading front near the splat periphery cools down to a temperature lower than that causing fusion of the underlying Al substrate. As the spreading melt moves out of the melted crater in a direction parallel to the substrate surface, its inertia may cause the spreading melt to lift off the substrate.

Numerical simulation [9] informs that the substrate surface melting and re-solidification occur very fast. This will generate quenching stress and a very weak physical bond will either be completely absent or present just in those areas of the splat−substrate interface where no metallurgical bond is formed [15]. One thing that should be taken into consideration is that such numerical simulation predicts the melting of solid Al surface by the impact of pure Al splat without the oxidized one. However, Al particles will get oxidized during APS, and splat impact-induced melting will be hindered at those regions where a thin oxide scale exists.

3.3 Microstructure of Al−WC coating

The cross-sectional SEM images of APS prepared Al−WC coating are shown in Figs. 4(a, b). It can be seen that the coating is dense without visible pores or gaps between adjacent splats. It can be also found that the coating is composed of three phases with different profiles and contrasts. Figure 4(c) shows the XRD pattern of Al−WC composite coating in comparison with Al−WC powder. It was recognized that the phases of W_2C and WAl_{12} are present in the coating besides Al and WC. This means that the decarburization of WC to W_2C occurred during spray deposition, while the presence of WAl_{12} could be attributed to the reaction of Al matrix to WC. The TEM examination confirmed the presence of the WAl_{12} phase in the coating at the interface region between the Al matrix and WC particle, as shown in Fig. 5, by TEM image and diffraction pattern. It is worth noting that diffraction peaks corresponding to any crystalline phases of alumina were absent. This fact suggests that oxidation of Al that always occurs in thermally sprayed Al or Al-alloy coatings could be greatly minimized or eliminated by adding WC. Such a phenomenon could be attributed to the decarburization of WC during spray. As compared to Al, the C element could react with oxygen preferentially. Since the decarburization product CO is gaseous, oxide-free droplets could be achieved under optimized conditions.

Moreover, a broad peak was also present in the XRD pattern around WAl_{12} peak at 2θ of about 40°. It could be attributed to the formation of amorphous or nanocrystalline phases formed at a very high cooling rate. In plasma spray, the cooling rate of the droplet could exceed 10^5 K/s during splat cooling and metastable phases can be formed in the coating [16]. Therefore, the coating was annealed in an inert argon atmosphere for 8 h at 400 °C to crystallize possible metastable phases in the coating. In Fig. 4(d), it can be seen that the broad peak disappeared to have evolved into a sharp one corresponding to that of WAl_{12}. This fact reveals that part of the matrix phase had Al alloyed with tungsten. Such alloying could result from the dissolution of WC or W_2C into molten Al at high temperatures. The capacity of Al alloy to become amorphous is enhanced by alloying with refractory elements. Thus, the amorphous phase was present in the Al−WC coating as was found in thermally

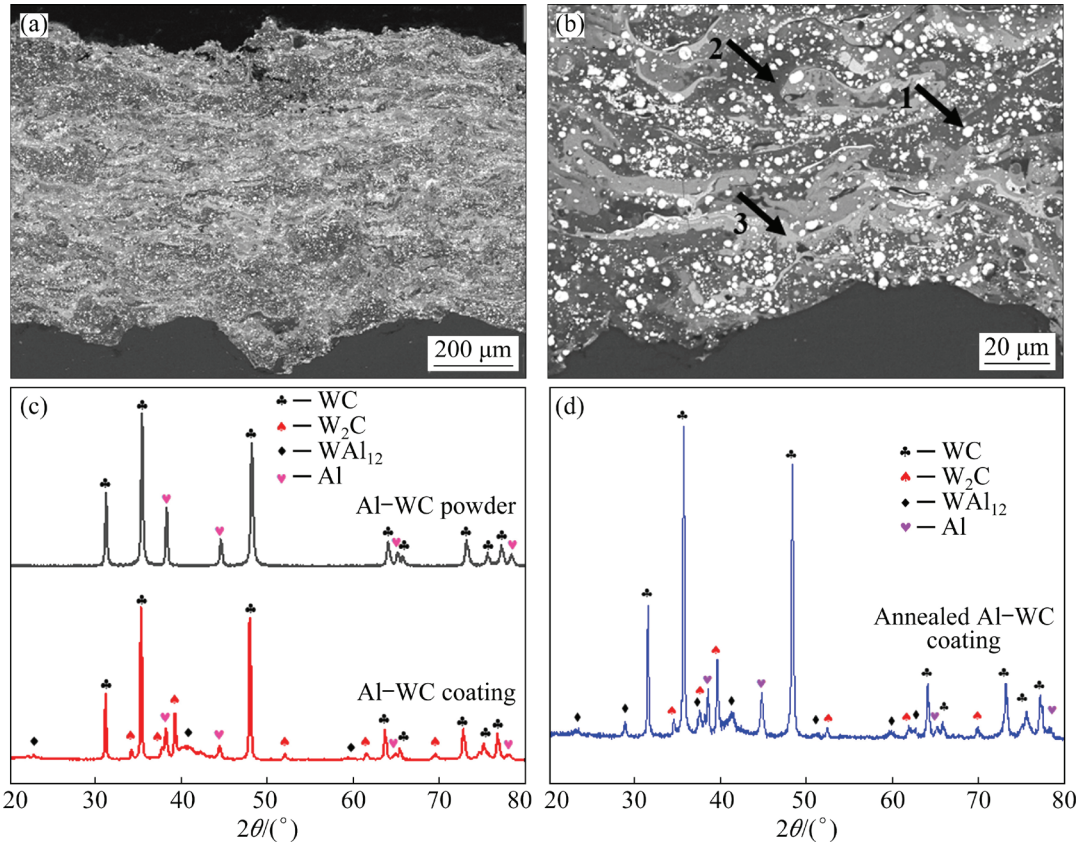

Fig. 4 Cross-sectional images of Al−WC coating on Mg at different magnifications with typical phase indications (WC particle (1), Al phase (2) and amorphous phase region (3)) in Al−WC coating (a, b), and XRD patterns of Al−WC powder and coating (c) and annealed Al−WC coating (d)

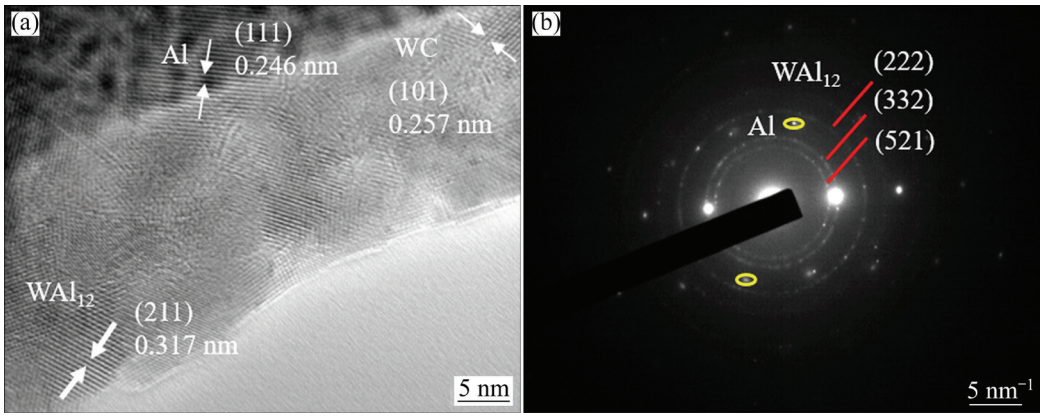

Fig. 5 TEM image of Al−WC coating (a) and selected area electron diffraction pattern (b)

sprayed WC−Co coatings [17].

The decarburization of WC during plasma spray in the present work could be similar to that in thermal spraying of WC−Co cermet coatings [18]. Basically, there are three mechanisms for carbide decarburization when spraying WC-based cermet: dissolution of carbide into the molten metal binder matrix, thermal decomposition of WC into W_2C, and oxidation-assisted decarburization [19].

Accordingly, the decarburization may occur through the following four major reactions:

$$2WC=W_2C+C \quad (1)$$

$$2WC+O_2=W_2C+CO_2 \quad (2)$$

$$2W_2C+O_2=2W_2(CO) \quad (3)$$

$$W_2(CO)=2W+CO \quad (4)$$

The thermal decomposition of WC to W_2C

occurs at a temperature higher than 2620 °C. It makes sense that the creation of W_2C results from the WC oxidation-assisted decarburization when taking into account the measured particle temperature, as shown in Fig. 2. The resultant W_2C may subsequently transform to metallic W when high temperature is attained in an oxygen-rich atmosphere [20]. The above oxidation reactions of WC consume a certain amount of active oxygen and thus minimize or avoid the oxidation of the Al element in the in-flight particle. Moreover, the dissolution of WC into molten Al leads to the presence of free carbon in spray particle, which benefits deoxidizing of in-flight particle.

Figure 6 shows cross-sectional microstructure of the APS prepared Al coating at two different magnifications which was etched to present the oxide distribution in the coating. The estimation yielded an apparent porosity of 0.04% for Al−WC coating in comparison with 3.88% in Al coating. This result is lower than previously reported porosity in aluminum coatings deposited by high-efficiency supersonic plasma spraying (1.02% in porosity) and oxygen–acetylene flame spraying (2.18% in porosity) and shot peening assisted cold spray Al coatings (0.4% in porosity) [21,22]. As shown later, such low porosity endows the Al−WC coating with the possibility of full protection for metal substrate from corrosion.

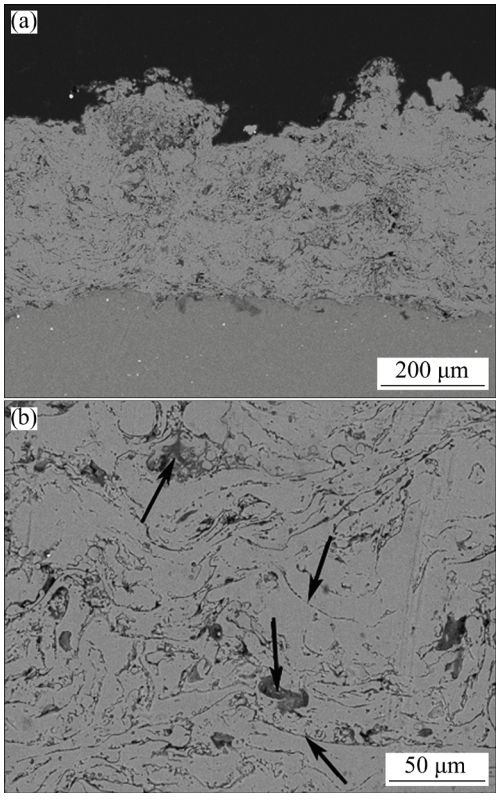

Fig. 6 Cross-sectional microstructure of pure Al coating on Mg substrate (a), and oxides in Al coating indicated by black arrows (b)

As shown in the previous section, since most spray particles reached a temperature higher than 1800 °C, the condition for the spread-fusing self-metallurgical bonding mechanism was fulfilled. Thus, when an Al−WC particle impacts on the previously deposited Al−WC splats, metallurgical bonding can be formed between Al matrix at the adjacent splat interface through spread-fusing. Another factor that makes Al−WC coating denser is the lowered thermal conductivity of Al−WC coating as compared with pure Al coating. By taking account of the thermal conductivity of 205 $W \cdot m^{-1} \cdot K^{-1}$ for Al and 110 $W \cdot m^{-1} \cdot K^{-1}$ for WC, the thermal conductivity of Al−WC coating will be lower than that of pure Al. Thus, the effusivity of Al−WC coating is lower than that of pure Al. As a result, the maximum substrate−splat interface temperature becomes high when Al−WC particle impacts on previously deposited splats as compared with Al coating. Consequently, the formation of the metallurgical bonding between splat interfaces can be further promoted.

As mentioned previously, the oxidation of WC occurs during the APS of Al−WC coating. Such a reaction could reduce active oxygen surrounding in-flight spray particle and thus oxidation of Al matrix phase, resulting in reduced oxides inclusion in the coating. As a result, more Al−WC spray particle may spread over fresh Al matrix without oxides. This effect could also enhance the formation of metallurgical bonding. Inter-lamellar pores are significantly reduced as the result of the establishment of the metallurgical bonding.

Another typical feature of Al−WC spray particles different from the pure Al droplet is its solid−liquid two-phase state since the Al matrix is in molten state while WC particles are kept at solid state. The solid WC particles in Al−WC increase the equivalent viscosity of Al−WC particle significantly. This significantly reduces the splat size due to increased viscosity and subsequently increases interface fraction where high transient pressure acts. Moreover, the high density of carbides (15.63 g/cm^3 for WC, 17.34 g/cm^3 for W_2C vs 2.7 g/cm^3 for Al) leads to an increase in the

apparent density of Al−WC particles, which further results in higher transient impact pressure. Furthermore, impact of high-density solid WC particles within Al−WC particle could cause peening effect, which not only densifies the previously deposited splat layers to close possible small pores but also breaks surface oxide scale to promote metallurgical bonding. As a result, the limited splat size, high impact pressure, and potential in-situ peening effect all help to generate the dense Al−WC coating.

3.4 Bond strength of Al−WC coatings

One of the essential characteristics of protective coatings is adherence, which determines the durability of the coatings. The tensile test yielded a mean tensile (adhesion/cohesion) strength of 32.3 MPa for Al−WC coatings in comparison with the value of 33.7 MPa for pure Al coating. It was observed that both the coatings fractured near the interface. Figure 7 shows the fracture surface morphologies of Al−WC coating observed at the both Mg alloy substrate side and the coating side. On the substrate side, the image taken in the BSE mode clearly presents a very high contrast. It was confirmed by EDS analysis that Mg was present in the regions in a dark contrast and WC was present in the regions in a bright contrast. This suggests that substantial splats were attached to the fracture surface at the substrate side. On the other hand, a small amount of Mg was found on the coating side. From the XRD analysis of the fractured interface at the coating side, as shown in Fig. 7(c), it can be clearly observed that besides the phases observed in the Al−WC coatings the intermetallic compound phases such as $Al_{12}Mg_{17}$. $Al_{18}Mg_3W_2$ and $Al_{0.58}Mg_{0.42}$ are also present. This fact indicates that the metallurgical reaction between the melted substrate and molten splat occurred during the spreading of the molten Al−WC droplet. However, due to the brittle feature of intermetallic phases, the test only yielded a strength value of 32.3 MPa. It is worth noting that although the adhesive strength of Al−WC coating is equivalent to that of the pure Al coating, the adhesive strength values in the present work are higher than the previously reported value of 21 MPa for plasma-sprayed Al coating by KUBATÍK et al [23].

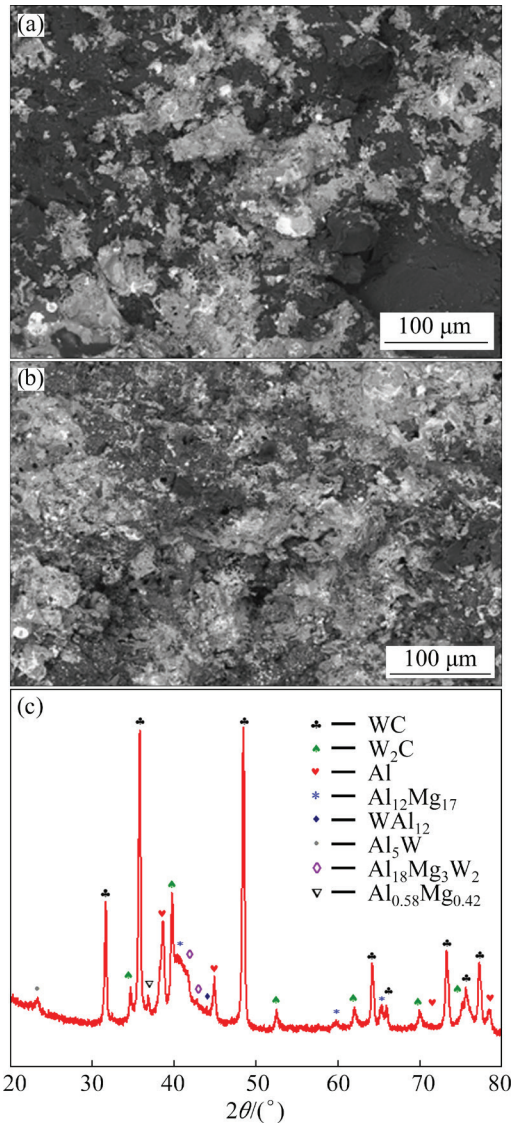

Fig. 7 SEM images of fractured interface of Al−WC coating in BSE mode from substrate side (a) and coating side (b); XRD pattern of fractured Al−WC coating interface at coating side (c)

3.5 Corrosion behavior of APS prepared Al−WC coatings

The electrochemical corrosion behavior of the coatings placed on Mg alloy substrates was used to assess the protective impact of APS Al−WC coating for metal substrates against corrosion. Since magnesium is anodic with respect to aluminum, the existence of any through-thickness pore can be detected through comparing the results for coated sample, bulk coating and bare substrate. The open circuit potential (OCP) and potentio-dynamic polarization (PDP) curves of Al−WC coating are shown in Figs. 8(a, b), in comparison with bulk Al, bulk Mg and Al-coated Mg alloy as well. It can be

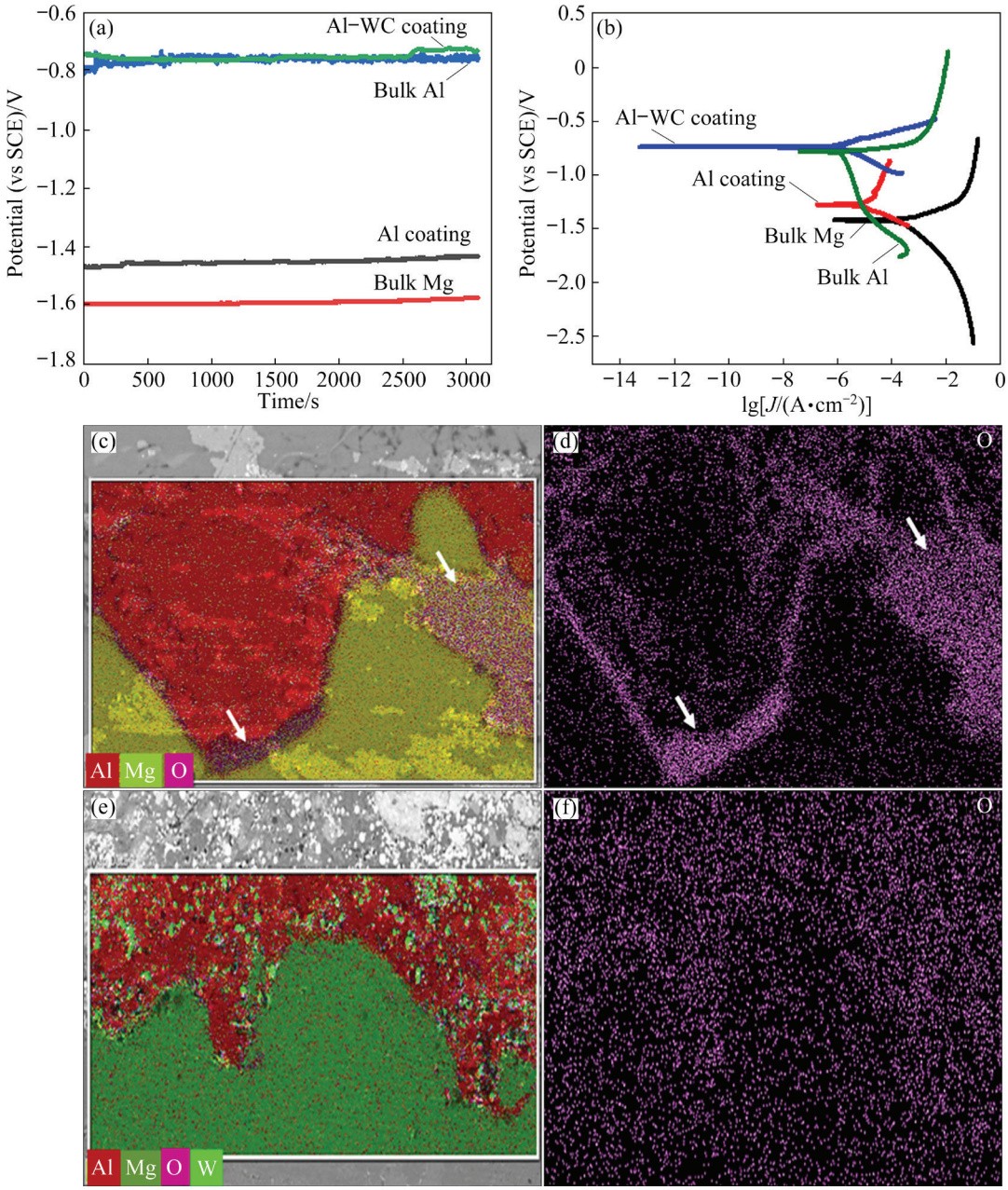

Fig. 8 OCP (a) and PDP (b) curves of Al and Al−WC coatings in comparison with bulk Al and bulk Mg; EDS elements mapping (c) at interface region of Al coating on Mg alloy after 900 h in salt fog; oxide clusters at coating−substrate interface (d); EDS elements mapping (e) at interface region of Al−WC coating on Mg alloy after 900 h in salt fog; No cluster of oxides at coating−substrate interface (f)

observed that the OCP and PDP curves of the Al−WC coated Mg alloy are comparable to those of bulk Al, while those of the pure Al-coated alloy are far deviated from those of bulk Al and shift towards those of bulk Mg. EDS maps of the interface regions of Al coating and Al−WC coating on AZ31B Mg alloy substrate, after being exposed to 5 wt.% NaCl neutral salt-fog spray for 900 h, are shown in Figs. 8(c, d) and Figs. 8(e, f), respectively. Oxide clusters are clearly visible at the coating−substrate interface of Al coating, as pointed by white arrows in Figs. 8(c, d), while no oxide clusters are observed at the coating−substrate interface of Al−WC coating. These data clearly indicate that there are no through-thickness pores in the APS prepared Al−WC coating. Thus, the electrolyte could not penetrate the coating and the electrochemical behavior of the coated sample is determined by the coating itself despite of the substrate material property. On the other hand, it

can be seen that the OCP of Al coating is lower than that of bulk Al. This shift from the OCP of bulk Al towards that of bulk Mg indicates the presence of through-thickness pores in the Al coating. The through-thickness pores permit the corrosive fluid to penetrate the coating to the interface between the coating and the substrate and corrode Mg. As a result, the corrosion behavior is governed by the electrochemical behavior of the substrate. Accordingly, the PDP curve of Al-coated Mg alloy shows similarity with that of bulk Mg alloy.

Table 2 presents the values of φ_{corr} and J_{corr} obtained by Tafel extrapolation from the PDP curves. It is evident that the corrosion potential (φ_{corr}) of Al-coated Mg alloy is lower than that of bulk Al and is close to that of bulk Mg. On the other hand, the corrosion potential (φ_{corr}) of Al−WC-coated Mg alloy is even slightly higher than that of bulk Al. As for the corrosion current, it can be noted that the corrosion current (J_{corr}) obtained for AZ31B in this study, shown in Table 2, is comparable to that reported for AZ31 alloy in literature. Moreover, for Al−WC-coated Mg alloy, J_{corr} is significantly lower than that of Mg alloy by about four orders of magnitude, and two orders of magnitude lower than that of bulk Al [24,25]. The significantly low corrosion rate could be attributed to the fine microstructure of Al−WC coating with tungsten alloyed amorphous matrix phases.

Table 2 Corrosion potential and corrosion current density by Tafel extrapolation

Sample	φ_{corr}(vs SCE)/V	J_{corr}/(A·cm^{-2})
Bulk Mg	−1.45	9.63×10^{-5}
Bulk Al	−0.78	1.16×10^{-6}
Al coating	−1.27	1.07×10^{-6}
Al−WC coating	−0.74	3.54×10^{-8}

3.6 Wear behavior of plasma sprayed Al−WC coatings

The wear resistance of the resultant composite coating was examined by a ball-on-disk wear test with alumina as the wear counterpart. The coefficients of friction (COFs) of both the coatings and bulk substrate (AZ31B Mg alloy) are shown in Fig. 9 against wear cycle number. At the early stage, the COF of Al−WC coating is lower than that of bulk Mg and it increases slightly up until almost 1000 cycles and then becomes close to that of bulk Mg. This slight initial rise may be caused by the newly formed wear debris. On the other hand, the COF of Al coating presents significant fluctuation. This fluctuation can be attributed to the formation and spalling of oxide wear debris on the coating surface. The COF of Al−WC coating is lower than that of Al coating, which can be attributed to the dispersion of WC particles and intermetallic phases in the coating. The average hardness of Al−WC coating is $HV_{0.5}$ 1400, while the average hardness of Al coating is $HV_{0.025}$ 39. Higher hardness leads to a smaller contact area and lower COF. The WC particles and intermetallic phases not only increase the hardness of the coating but also reduce the chemical affinity with the alumina ball wear counterpart.

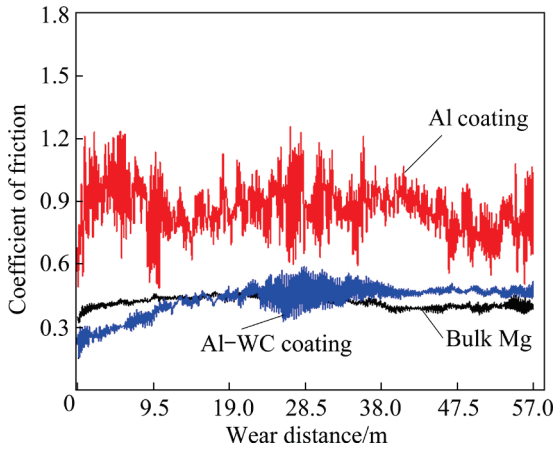

Fig. 9 Friction coefficient vs wear distance of samples

The surface images of wear tracks on Al coating, Al−WC coating and Mg alloy are shown comparatively in Figs. 10(a−c), respectively. Under the same wear load of 5 N on all three samples, the wear track on Al−WC coating is the thinnest as compared to Al coating and Mg substrate. Table 3 presents the mass loss, calculated volume loss and widths of wear tracks. It is evident from the surface images of wear tracks, volumetric loss and width of wear tracks that Al−WC coating presents a better wear resistance as compared to both the Al coating and Mg alloy substrate. The wear loss of Al−WC coating is about one order of magnitude lower than that of both Mg alloy substrate and Al coating. In the Al−WC cermet coating, the hard WC and W_2C particles limit the plastic deformation of soft Al matrix, which results in constraining the metallic matrix. Moreover, the formation of WAl_{12} phase at the interface between Al matrix and WC particle

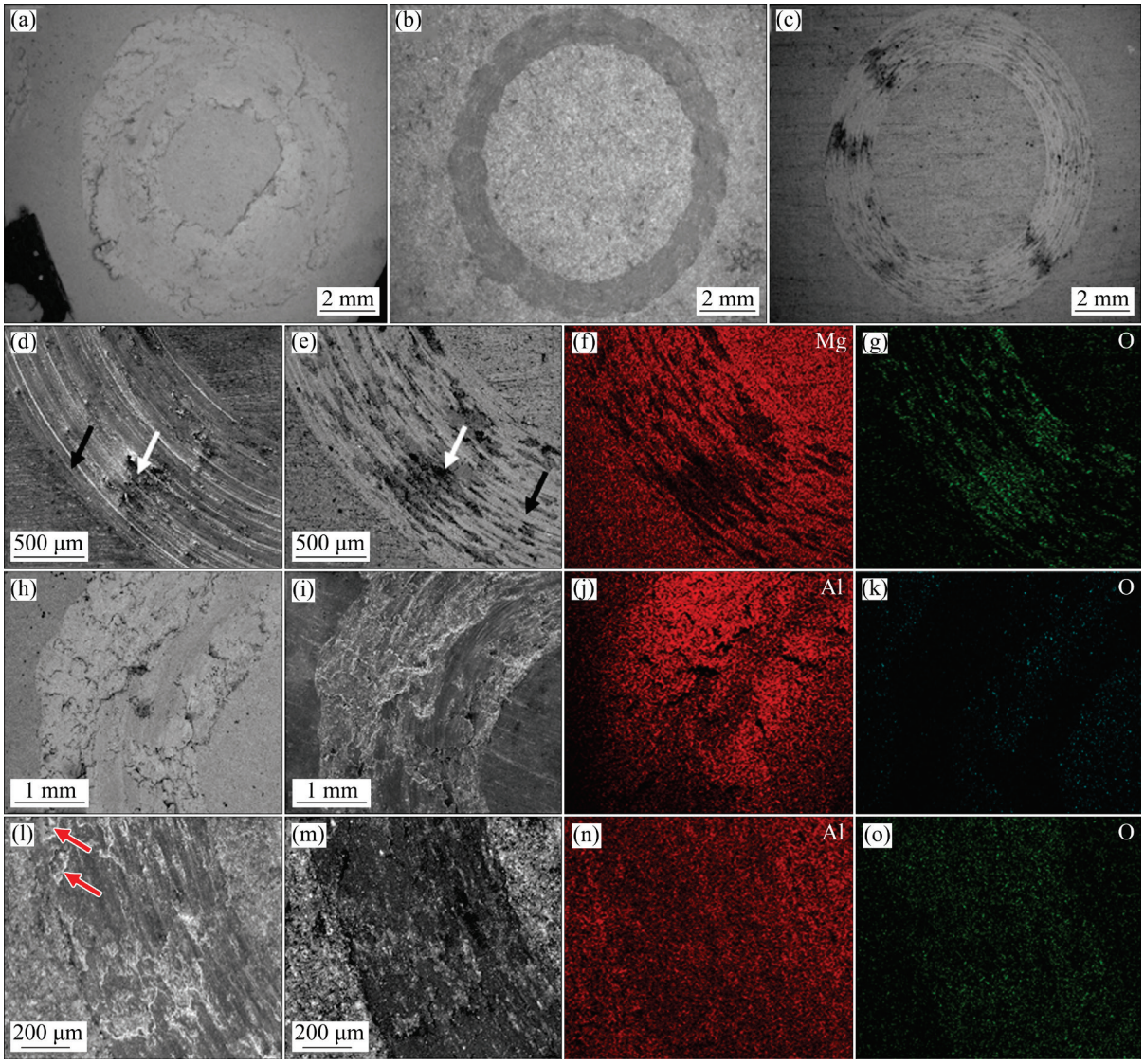

Fig. 10 Wear tracks on different samples ((a) Al coating, (b) Al−WC coating, and (c) Mg substrate); Typical wear track on Mg substrate ((d) SE mode image, and (e) BSE mode image); EDS mappings and of Mg (f) and O (g) on typical wear track on Mg substrate; Typical morphology of wear track on Al coating ((h) SE mode image, and (i) BSE mode image); EDS mappings and of Al (j) and O (k) on typical wear track on Al coating; Typical morphology of wear track on Al−WC coating ((l) SE mode image, and (m) BSE mode image); EDS mappings and of Al (n) and O (o) on typical wear track on Al−WC coating

Table 3 Mass loss, calculated volume loss during wear and width of wear tracks

Material	Mass loss/g	Volume loss/cm^3	Width of wear track/mm
Mg substrate	0.015	8.79×10^{-3}	2.062
Al coating	0.024	8.85×10^{-3}	3.546
Al−WC coating	0.003	7.40×10^{-4}	1.311

results in a strong bonding between WC reinforcement phase and Al matrix. Such a strengthening effect reduces the possibility of pull-out or spalling of WC particles during abrasion [26].

The wear of Mg alloy occurred through a corrosive and abrasive mechanism. As shown in Figs. 10(d, e), the oxides indicated by the white arrows can be clearly observed in the abrasive wear grooves on the surface of the wear track on Mg alloy, being confirmed by the EDS mappings in Fig. 10(f). The increase of the surface temperature resulting from the friction promotes the oxidation of Mg alloy. The continuous abrasion results in removal of the oxide film, which is followed by the formation of a new oxide film. Oxide scale removed from the oxidized surface of Mg and trapped between the sliding

surfaces increases the wear rate by the three-body abrasive wear mechanism. Therefore, the mass loss is accelerated by the oxidation of Mg alloy. The wear track on the Al coating is shown in Figs. 10(g, h). Due to the extreme ductility and softness of Al, it seems highly plastically deformed as one may anticipate. Some furrows are visible in the wear track, voids and cracks are also present, wear debris are also present and edges of wear track are irregular in shape due to the extrusion of oxides. These surface features suggest that the wear mechanism is a combination of oxidation, abrasive, and delamination wear mechanisms.

The irregular shape of the sides of wear path evidences the material removal because of lamella spallation. Delamination seems to dominate wear in this case. As shown in the cross-sectional image of Al coating, pores, voids and oxides are present in Al coating. These defects weaken the inter-lamellar bonding. When Al coating is subjected to repeating compressive and tensile stresses resulting from applied normal load and friction during wear test, small cracks initiate, accumulate and result in delamination. From the EDS map of the wear track of Al coating shown in Fig. 10(i), the oxidation occurred due to heat resulting from friction. The substrate element Mg was found in several wear regions in the middle of the wear track, indicating that the wear track was deep enough to almost approach the coating−substrate interface.

The morphology of the wear track of Al−WC coating with typical EDS element mapping is shown in Figs. 10(j, k) and Fig. 10(l), respectively. The local layer delamination was obviously observed (indicated by red arrows in Fig. 10(j)), which could be attributed to the spalling of splats from weakly bonded interfaces. The EDS mapping confirmed the presence of oxides on the surface. Such oxides can result from the oxidation of the coating surface exposed to abrasion which caused local temperature rise by friction. Moreover, the oxygen observed on the surface exposed after delamination could result also from the oxides included at the lamellar interface during coating deposition. Under repeated loading during wear test, the gaps at the cracks between poorly bonded splats could have propagated parallel to the lamellar interfaces of the coating, which might have caused some parts of the splats to delaminate. There is less plastic deformation than that with a pure Al coating because there appears to be less material flow. Moreover, the sides of the wear track are comparatively smooth, indicating the absence of adhesive wear as the case in Al coating. Therefore, the wear of Al−WC coating occurs through a combined effect of abrasion, delamination and corrosive wear.

4 Conclusions

(1) Due to the deoxidization and self-metallurgical bonding effect of the superhot Al−15vol.%WC particles, the Al−WC cermet coating presents a dense microstructure without evident oxide scale inclusions. The formation of $Al_{12}W$ phase could enhance the bonding between Al matrix and WC particles.

(2) The Al−15vol.%WC provides long-term corrosion protection for the AZ31B Mg alloy and no corrosion production is formed at the coating−substrate interface after 900 h of salt-fog spraying corrosion. The electrochemical corrosion test reveals that the corrosion current density of the present coating is two orders of magnitude lower than that of pure Al bulk due to the formation of the amorphous phase.

(3) Due to the much high hardness of the plasma sprayed Al−15vol.%WC coating of HV 1400, it reveals one order of magnitude lower volumetric loss as compared to the plasma sprayed Al coating and Mg alloy substrate.

CRediT authorship contribution statement

Haroon RASHID: Investigation, Methodology, Date curation, Data analysis, Writing − Original draft, Writing − Review & editing; **Xiao-tao LUO:** Supervision, Data analysis, Writing − Review; **Xin-yuan DONG:** Methodology, Exprimentals; **Li ZHANG:** Methodology, Tests; **Chang-jiu LI:** Conceptuation, Funding acquisition, Supervision, Writing − Review & editing.

Declaration of competing interest

The authors declare that they have no known competing financial interests or personal relationships that could have appeared to influence the work reported in this paper.

Acknowledgments

The present work was supported by the National

Nature Science Foundation of China (Nos. 52031010, U1837201). One of the authors, Haroon RASHID, would like to express his appreciation to the Chinese Scholarship Council (CSC) for support of the scholarship.

References

[1] ZHANG W Y, DU Y H, PENG Z Z. Excellent plasma electrolytic oxidation coating on AZ61 magnesium alloy under ordinal discharge mode [J]. Journal of Magnesium and Alloys, 2022, 10(9): 2460−2474.

[2] HU J J, LIAO J, YANG X, ZENG J, LI H, SONG B, XU H B, GUO N, JIN Y. Microstructure and properties of Al-coating on AZ31 magnesium alloy prepared by pack-cementation [J]. Transactions of Nonferrous Metals Society of China, 2022, 32(2): 493−502.

[3] THIRUMALAIKUMARASAMY D, KAMALAMOORTHY K S, VISVALINGAM V B. Effect of experimental parameters on the micro hardness of plasma sprayed alumina coatings on AZ31B magnesium alloy [J]. Journal of Magnesium and Alloys, 2015, 3(3): 237−246.

[4] DAROONPARVAR M, BAKHSHESHI-RAD H R, SABERI A,RAZZAGHI M, KASAR A K, RAMAKRISHNA S, PRADEEP L, MENEZES, MISRA M, ISMAIL A F, SHARIF S, BERTO F. Surface modification of magnesium alloys using thermal and solid-state cold spray processes: Challenges and latest progresses [J]. Journal of Magnesium and Alloys, 2022, 10(8): 2025−2061.

[5] FAN C H, HE W J, HU Z Y, WU Q, NI Y M. Interface structure and properties of spray-forming (SiC_p + β-$LiAlSiO_4$)/6092Al matrix composites [J]. Transactions of Nonferrous Metals Society of China, 2023, 33(4): 1029−1037

[6] VERDIAN M M, HASHMI M S J. Finishing and post-treatment of thermal spray coatings [M]. Comprehensive Materials Finishing. Amsterdam: Elsevier, 2017: 191−206.

[7] HIRAGA H, INOUE T, SHIMURA H, AKIRA M. Cavitation erosion mechanism of NiTi coatings made by laser plasma hybrid spraying [J]. Wear, 1999, 231(2): 272−278.

[8] HIRAGA H, INOUE T, KAMADO S, Y KOJIMA, AKIRA M, HIROFUMI S. Fabrication of NiTi intermetallic compound coating made by laser plasma hybrid spraying of mechanically alloyed powders [J]. Surface and Coatings Technology, 2001, 139(1): 93−100.

[9] LI C J, LUO X T, DONG X Y, L ZHANG, LI C X. Recent research advances in plasma spraying of bulk-like dense metal coatings with metallurgically bonded lamellae [J]. Journal of Thermal Spray Technology, 2022, 31: 5−27.

[10] DONG X Y, LUO X T, ZHANG S L, LI C J. A novel strategy for depositing dense self-fluxing alloy coatings with sufficiently bonded splats by one-step atmospheric plasma spraying [J]. Journal of Thermal Spray Technology, 2020, 29(1): 173−184.

[11] DONG X Y, LUO X T, GE Y, LI C J. Enhancing the hot-corrosion resistance of atmospheric plasma sprayed Ni-based coatings by adding a deoxidizer [J]. Materials & Design, 2021, 211: 110154.

[12] ZENG Z, KURODA S, ERA H. Comparison of oxidation behavior of Ni−20Cr alloy and Ni-base self-fluxing alloy during air plasma spraying [J]. Surface and Coatings Technology, 2009, 204(1/2): 69−77.

[13] ZHANG L, WANG D, LIAO X J, LUO X T, LI C J. The influence of diamond addition to Ni-Al powder on oxidation behavior of NiAl during plasma spraying for high performance oxide-free Ni−Al intermetallic coating [C]// Proceedings of the International Thermal Spray Technology. Portugal, 2021.

[14] LI C J, LI C X, YANG G J, WANG Y Y. Examination of substrate surface melting-induced splashing during splat formation in plasma spraying [J]. Journal of Thermal Spray Technology, 2006, 15(4): 717−724.

[15] YAO S W, LI C J, TIAN J J, YANG G J, LI C X. Conditions and mechanisms for the bonding of a molten ceramic droplet to a substrate after high-speed impact [J]. Acta Materialia, 2016, 119: 9−25.

[16] MCPHERSON R. Formation of metastable phases in flame-and plasma-prepared alumina [J]. Journal of Materials Science, 1973, 8(6): 851−858.

[17] LI C, OHMORI A, HARADA Y. Formation of an amorphous phase in thermally sprayed WC−Co [J]. Journal of Thermal Spray Technology, 1996, 5(1): 69−73.

[18] YUAN J, ZHAN Q, HUANG J, DING S Y, LI H. Decarburization mechanisms of WC−Co during thermal spraying: Insights from controlled carbon loss and microstructure characterization [J]. Materials Chemistry and Physics, 2013, 142(1): 165−171.

[19] LI C J, OHMORI A, HARADA Y. Effect of powder structure on the structure of thermally sprayed WC−Co coatings [J]. Journal of Materials Science, 1996, 31(3): 785−794.

[20] TU D, CHANG S, CHAO C, LIN C. Tungsten carbide phase transformation during the plasma spray process [J]. Journal of Vacuum Science & Technology, 1985, 3(6): 2479−2482.

[21] WEI Y K, LUO X T, LI C X, LI C J. Optimization of in-situ shot-peening-assisted cold spraying parameters for full corrosion protection of Mg alloy by fully dense Al-based alloy coating [J]. Journal of Thermal Spray Technology, 2017, 26(1): 173−183.

[22] JIN Z A, LIU M, ZHU L N, WANG H D, MA G Z, XING Z G, KANG J J, CHEN S Y. Microstructure and corrosion behavior of aluminum coatings prepared by high-efficiency supersonic plasma spraying and oxygen–acetylene flame spraying [J]. Journal of Thermal Spray Technology, 2020, 29(3): 489−499.

[23] KUBATÍK T F, PALA Z, NEUFUSS K, VILÉMOVÁ M, MUŠÁLEK R, STOULIL J, SLEPIČKA P, CHRÁSKA T. Metallurgical bond between magnesium AZ91 alloy and aluminum plasma sprayed coatings [J]. Surface and Coatings Technology, 2015, 282: 163−170

[24] SINGH I, SINGH M, DAS S. A comparative corrosion behavior of Mg, AZ31 and AZ91 alloys in 3.5% NaCl solution [J]. Journal of Magnesium and Alloys, 2015, 3(2): 142−148.

[25] LUO X T, WEI Y K, SHEN J H, MA N, LI C J. Breaking the trade off between corrosion resistance and fatigue lifetime of the coated Mg alloy through cold spraying submicron-grain

Al alloy coatings [J]. Journal of Magnesium and Alloys, 2023, http://doi.org/10.1016/j.jma.2022.12.011.

[26] WANG P, ECKERT J, PRASHANTH K G, WU M W, KABAN I, XI L X, SCUDINO S. A review of particulate-reinforced aluminum matrix composites fabricated by selective laser melting [J]. Transactions of Nonferrous Metals Society of China, 2020, 30(8): 2001−2034.

添加 WC 颗粒对镁合金表面等离子喷涂 Al 基涂层耐腐蚀和耐磨损性能的影响

Haroon RASHID，雒晓涛，董昕远，张 黎，李长久

西安交通大学 材料科学与工程学院 金属材料强度国家重点实验室，西安 710049

摘 要：常规热喷涂工艺制备的金属涂层内的粒子界面弱结合导致其不能为基材提供长效的腐蚀防护，因此，采用大气等离子喷涂，实现粒子间的冶金结合，制备高致密 Al−15%WC(体积分数)复合涂层。 结果表明，由于 WC 颗粒中 C 元素的去氯效应，以及超高温熔滴(>1800 ℃)间的自冶金结合，在最优等离子喷涂条件下制备出无氧化物杂质的涂层。涂层的致密结构使其表现出优异耐腐蚀性能，其腐蚀电流密度比镁合金基体降低 4 个数量级，比纯铝块材降低 2 个数量级。WC 硬质颗粒的添加使 Al−WC 复合涂层的耐磨损性能相较纯 Al 块材提高 1 个数量级。

关键词：大气等离子喷涂；Al−WC 涂层；自冶金结合；去氧效应；耐腐蚀性；耐磨性

(Edited by Bing YANG)